International Journal of Advanced Technology and Engineering Exploration, Vol 12(123)
ISSN (Print): 2394-5443 ISSN (Online): 2394-7454
http://dx.doi.org/10.19101/IJATEE.2024.111100375

Research Article

NeuroPET: advancing breast cancer detection with an optimized deep convolutional spiking neural network

S. Tharani[1*] and R. Khanchana[2]
Research Scholar, Department of Computer Science, Sri Ramakrishna College of Arts & Science for Women, Coimbatore[1]
Associate Professor, Department of Computer Science, Sri Ramakrishna College of Arts & Science for Women, Coimbatore[2]

Received: 25-March-2024; Revised: 04-February-2025; Accepted: 22-February-2025
©2025 S. Tharani and R. Khanchana. This is an open access article distributed under the Creative Commons Attribution (CC BY) License, which permits unrestricted use, distribution, and reproduction in any medium, provided the original work is properly cited.

Abstract
Breast cancer (BC), a heterogeneous disease, remains the second leading cause of cancer-related mortality among women globally. The development of effective treatment strategies and the identification of critical biomarkers capable of predicting cancer progression remains challenging due to the diverse characteristics of BC. While positron emission tomography (PET) and molecular imaging (MI) have enhanced the characterization of BC, these techniques still face certain limitations. Recently, deep learning (DL) methods have revolutionized medical imaging by enabling the detection and analysis of features often imperceptible to the human eye. To address these limitations, NeuroPET, a novel framework, was proposed to enhance the accuracy and reliability of PET imaging for BC detection and classification. NeuroPET integrates several advanced methods, including the dynamic grade weighted switching median filter (DGWSMF), designed to mitigate impulsive noise in colour digital images, and a novel spatial adaptive fuzzy c-means (SAFCM) clustering method, developed to segment affected regions in PET scan datasets. At the core of NeuroPET is the optimal deep convolutional spiking neural network (ODCSNN), which employs direct training for PET image classification. The network's weights are optimized using the adaptive nut-finding algorithm (ANFA), enabling superior performance. NeuroPET further utilizes the gradient surrogate method to achieve a high classification accuracy of 95.02%, surpassing traditional approaches. Comparative analysis demonstrates that NeuroPET significantly outperforms existing techniques, underscoring its potential as an advanced BC detection, classification, and analysis tool.

Keywords
Machine learning (ML), Breast cancer (BC), Positron emission tomography (PET), Data mining (DM).

1.Introduction
Breast cancer (BC) represents a significant health concern among women in India, comprising approximately 27% of all cancers diagnosed in women [1]. The incidence of BC has been steadily rising in urban and rural areas. Although BC can affect women of any age group, women older than 40 are the individuals being diagnosed with it most frequently. However, there is an increasing incidence among younger women [2]. Despite being the most common cancer in Indian women [3], BC survival rates remain relatively low due to late-stage diagnosis and limited access to healthcare facilities, contributing to its status as the primary factor in women's cancer-related mortality.

Limited awareness, cultural barriers, and restricted access to screening programs hinder early detection efforts [4]. Efforts by the Indian government and organizations aim to raise awareness, promote early detection through screening, and improve access to quality treatment services to alleviate the burden of BC in India [5]. Accurate staging and early discovery are essential for effective therapy and better outcomes for patients. BC is among many malignancies for which positron emission tomography (PET) scanning has become an effective diagnostic and monitoring technique [6]. In recent years, integrating PET imaging into clinical practice has transformed BC management in India.

PET is a powerful imaging technique used in medical diagnostics, particularly in oncology and neuroscience, to visualize metabolic processes within

*Author for correspondence

the body [7]. Deep learning (DL) and machine learning (ML) methods have begun revolutionizing the field of PET imaging, enhancing its capabilities in areas such as image reconstruction, noise reduction, and disease classification [8]. In image reconstruction, DL algorithms have shown promise in improving the quality of PET images by reconstructing them from fewer projections or lower-dose scans, reducing patient radiation exposure without compromising diagnostic accuracy.

Moreover, ML models [9] trained on large datasets of PET scans have demonstrated remarkable performance in disease classification and prognostic assessment. By leveraging DL architectures [10], such as convolutional neural networks (CNNs), these models can automatically extract meaningful features from PET images and accurately differentiate healthy tissues from diseased ones [11]. This capability holds immense potential for early disease detection, personalized treatment planning, and monitoring response to treatment in conditions such as cancer and neurodegenerative disorders [12].

Overall, the ML and DL techniques in PET imaging enhance the quality of PET scans and diagnostic accuracy and open new avenues for quantitative analysis, biomarker discovery, and precision medicine in clinical practice. Continued research and development in this interdisciplinary field promise to advance our understanding and use of PET imaging in healthcare. However, it's also worth noting that the effectiveness of DL in any application depends on factors such as data quality, model architecture, and training methodology. In some cases, DL may outperform traditional ML methods but not provide significant advantages in others [13].

There are still many obstacles to overcome in the field of BC detection despite substantial progress that has been reached. Standard imaging methods, such as mammography and ultrasound, have a high probability of false positives (FP) and false negatives (FN), which puts patients at risk of receiving unnecessary biopsies or a delay in receiving a diagnosis. Moreover, these techniques sometimes involve radiation exposure and may not always be easily accessible or affordable. Training spiking neural networks (SNNs) and integrating them with existing medical infrastructure poses challenges despite their energy efficiency and suitability for real-time applications [14].

Therefore, it's essential to evaluate the performance of DL in PET imaging for BC detection and diagnosis against alternative approaches, considering factors such as interpretability, computational efficiency, and generalization. Furthermore, interdisciplinary collaboration among medical imaging, ML, and oncology experts is crucial for developing and evaluating effective DL models in this domain.

The main contribution of this paper is the introduction of NeuroPET, a novel framework aimed at enhancing the accuracy and reliability of PET imaging for BC detection and classification. NeuroPET integrates multiple advanced methodologies to address PET image noise interference, segmentation, and classification challenges. A key component of NeuroPET is the dynamic grade weighted switching median filter (DGWSMF), which is proposed to reduce impulsive noise in colour digital images. This filtering technique effectively mitigates noise interference in PET scans, improving the accuracy of subsequent analysis steps. Additionally, NeuroPET incorporates a clustering algorithm, the spatial adaptive fuzzy c-means (SAFCM), specifically tailored for PET scan datasets. This algorithm provides an innovative approach to segment affected regions in PET images, facilitating the identification and delineation of regions associated with BC. Another major contribution of NeuroPET is developing the optimal deep convolutional spiking neural network (ODCSNN), a DL model designed to classify BC in PET images. This model leverages the strengths of deep CNNs and spiking neural network (SNN) elements to enhance efficiency and biological plausibility. To further enhance the performance of ODCSNN, the adaptive nut-finding algorithm (ANFA), a metaheuristic optimization technique, is employed. ANFA identifies the optimal set of parameters for ODCSNN, significantly improving its classification accuracy on PET images.

The remainder of this study is organized as follows: Section 2 reviews related studies. Section 3 provides a detailed explanation of the proposed method and framework. Section 4 presents a comprehensive performance analysis of the proposed methodologies. Finally, Section 5 concludes the study and outlines directions for future research.

2.Related work

This section offers an inclusive review of existing research on impulsive noise removal techniques in digital image processing, clustering algorithms for medical image segmentation, and DL approaches for BC classification using PET imaging. It highlights the gaps in the literature and sets the context for the proposed methodologies. Inglese et al. [15] employed the diagnostic capability of dynamic PET acquisitions of different lengths for differentiating BC lesions in the lack of blood vessel sampling compared with dynamic PET alone, using a range of DL algorithms. The disadvantage of various DL approaches for PET image BC classification is their susceptibility to overfitting due to limited or imbalanced datasets, potentially leading to reduced generalization performance in real-world clinical settings. Using dedicated breast positron emission tomography(dbPET) data from 458 breasts,109 BCs, and 349 non-BCs that included medial-lateral and craniocaudal maximum intensity projection (MIP) images, we accordingly trained an Xception-DL algorithm for identifying BC or non-BC. dbPET images in 160 breasts, 43 BC, and 117 non-BC were used to evaluate it. The disadvantage of using an Xception-based DL model for PET image BC classification could be its high computational complexity, which may limit its practical deployment in resource-constrained clinical environments.

Khodabakhshi et al. [16] goal was to develop radiomic algorithms for non-small cell lung cancer (NSCLC) subgroup classification and thoroughly assess the impact of ComBat harmonization on the effectiveness of single- and multimodality radiomic algorithms that are utilizing a dual-centre dataset. AdaBoost, logistic regression (LR), and support vector machines (SVM) were tested in ML to categorize NSCLC subgroups. The disadvantage of various ML approaches for PET image BC classification is their reliance on handcrafted features, which may limit their capability for intricate structure capitalization and variations in the data compared to DL methods.

Qiao et al. [17] suggested an (attentive transformation (AT)- normalization technique for PET tumor segmentation. To take advantage of the ability to distinguish breast tumours in PET images. The approach constantly generates geared and pixel-dependent learnable parameters within normalization through the transformation on the ensemble channel-wise and spatial-wise AT. The disadvantage of AT-normalization for PET image BC could be its sensitivity to variations in image quality and acquisition protocols, potentially leading to suboptimal performance in real-world clinical scenarios.

Imokawa et al. [18] proposed a U-Net-based model with an uptake shape classification head used. This was trained by both the original and an enriched dataset that included collage images. The simulations have been contrasted utilizing the Wilcoxon signed-rank test to determine the Dice score, which calculates the pixel-wise agreement between predicted and actual reality. Additionally, the accuracy of the classifications was assessed. The disadvantage of a U-Net-based model for PET image BC could be its potential vulnerability to overfitting, especially when dealing with limited or imbalanced datasets.

Tsukijima et al. [19] sought to improve image quality by reconstructing reduced time frames for acquiring information using DL as a noise reduction technique. The drawbacks of employing a deep denoising filter bank in a position-adaptive PET image noise reduction technique could be increased computational complexity, potentially limiting its real-time application in clinical settings.

Sueoka et al. [20] examined the sensitivity of whole-body positron emission tomography (WBPET) and PET (DbPET) in diagnosing invasive BC, considering tumour size and biology. A retrospective analysis was conducted to assess the sensitivity of DbPET and WBPET in detecting tumours and tumour biology based on clinicopathological characteristics.

Yurdusev et al. [21] created difference filter and YOLO-V4 DL model for mammogram detection and classification. The trials are rerun without the difference filter to demonstrate its role in the successful categorization. Because it highlights microcalcifications and makes rounded edges more visible, the neighbourhood relation-based difference filter greatly improves the classification success ratios of the study's classifier models. According to the results of the studies, using DL models in conjunction with the difference filter results in a substantial improvement in classification accuracy.

Nogales et al. [22] suggested a DL approach using evolutionary algorithms for BC diagnosis (DLA-EABA). Depending on the treatment performed on the images, the author of this research examines

several alternatives based on four distinct use cases. At this stage, several scenarios are generated, each with the potential to profit from sophisticated hybrid artificial intelligence models. In addition to evaluating the solutions, supply us with an accurate model, and it will offer it. Nevertheless, it will allow us to comprehend better how the various thermography results impact the diagnosis. Using a hybrid model consisting of CNN and evolutionary algorithms, the results demonstrate that it is possible to reach an accuracy of around 94% by splitting the thermography across three different temperature ranges.

Singh and Alam [23] proposed an Optimal faster region-based convolution neural network (OFRCNN) for the early detection of BC in digital mammograms. The Faster RCNN model has recently emerged as a formidable instrument for studying medical images in terms of object identification. When used alone, the Faster RCNN model has several drawbacks when detecting BC. Here are the areas of mass: Consequently, this study proposes a mass detection technique that uses pixel-based low-level preprocessing and a quicker RCNN approach to tackle the problem. Multiple metrics, including specificity, accuracy, sensitivity, and area under the curve (AUC), are used to assess the efficacy of the suggested method. The author compared the proposed model's performance to other DL-based models and state-of-the-art algorithms like region-based fully convolutional network (R-FCN) and single shot detector (SSD). Impressive sensitivity (95.2%), accuracy (94.2%), specificity (93.5%), and AUC (0.983) were all reached by the suggested method.

Thakur et al. [24] recommended the CNNs with optimized ReduceLROnPlateau and early stopping enhancements for BC diagnosis. An innovative CNN model that incorporates an early stopping callback and ReduceLROnPlateau callback is introduced in this study to meet the urgent demand for better BC diagnosis. Better patient outcomes and lower death rates are the project's ultimate goals, which attempt to improve BC classification accuracy and reliability to circumvent the shortcomings of current diagnostic tools. The versatile and dependable performance of the model in different clinical settings is highlighted by the thorough approach, which comprises a variety of datasets, careful picture preprocessing, intense model training, and validation procedures. With a 95.2% accuracy rate in differentiating between non-cancerous and cancerous breast tissue in the integrated dataset, the CNN model proved very effective, which bodes well for the future of AI-driven diagnostics and better clinical decision-making.

Munshi et al. [25] presented the optimized ensemble learning framework and explainable artificial intelligence (XAI) for BC detection. Predictions based on images are made using the U-NET transfer learning model. In addition, a bespoke CNN model is integrated with an ensemble consisting of random forest (RF) and SVM to produce an ensemble model. The experiments aim to examine the impact of simple and complex characteristics. Using the Wisconsin dataset, we compare several classifiers to see which ones best detect BC. With an impressive accuracy rate of 99.99%, the model being considered shows potential for improving BC diagnosis. By outlining a new ML-based approach and talking about how the variables might be interpreted using XAI, this work adds to the progress of BC diagnosis. Acquiring a remarkable degree of accuracy is the primary goal of this strategy, which will allow for the early and accurate detection of BC. The ultimate goal of this strategy is to improve patient health outcomes.

Chugh et al. [26] introduced the classical ML transfer learning paradigm for breast carcinoma diagnosis. In the first method, known as deep feature extraction (DFE) with ML classifier head, models from deep convolutional neural networks (DCNNs) like Res Net 50, Res Net 152, visual geometry group (VGG16), and VGG19 are used to extract features, which are then used to train traditional ML classifiers. The second method incorporates a neural network classifier for feature extraction (FE) and classification. It uses mobile net, VGG16, VGG19, ResNet50, Res Net 152, and dense Net 169. In the first scenario, the findings demonstrate that RF and eXtreme Gradient Boost (XGB) classifier do the best on the training set with a 100% accuracy rate, while SVM and XGB achieve 95% (+5%) accuracy on the test dataset across all models. In the second method, the models with the best accuracy 97% (+2%) on both the training and test sets) were mobile net, resnet50, and dense net 169. The second method shows a 4% improvement in accuracy, according to the assessed findings.

Raza et al. [27] suggested the DeepBraestCancerNet DL model for BC detection and classification. Six convolutional layers, nine inception modules, and a fully linked layer make up the 24 layers of the proposed system. The design also employs two

normalization operations: batch normalization, cross-channel normalization, and clipped and leaky rectifier linear unit (ReLu) activation functions. As we can see, the suggested model achieved a maximum classification accuracy of 99.35%. The experimental findings demonstrated that the proposed model surpassed the state-of-the-art when the author compared its performance with other DL models. Additionally, the author evaluated the DeepBraestCancerNet method and used another industry-standard, publicly available dataset to verify the suggested model. The suggested DeepBraestCancerNet model achieved a maximum accuracy of 99.63%.

Sahu et al. [28] recommended the high accuracy of hybrid CNN classifiers for BC detection using mammogram and ultrasound datasets. Hybrid systems that use both networks' strengths outperform their base classifiers. Furthermore, a threshold value and weight factor based on likelihood are critical for effective hybridization. A more precise and quicker system is achieved by using an optimal threshold value that has been determined experimentally. The suggested approach outperforms conventional DL techniques even with relatively limited datasets. Two datasets from several BC modalities, mini-DDSM (mammogram) and BUSI and BUS2 (ultrasound), are used to verify the suggested approach. The experimental findings show that the suggested ShuffleNet-ResNet technique outperforms the state-of-the-art approaches on all specified datasets. Furthermore, the proposed method gets 99.17% and 98.00% accuracy in mini-DDSM and 96.52% and 93.18% accuracy in BUSI datasets for abnormality and malignancy identification, respectively. BUS2 has a malignancy detection accuracy of 98.13%.

Emam et al. [29] proposed the optimized deep CNN based on the transfer learning technique and improved Coati optimization algorithm (COA) for BC detection and diagnosis. Lévy Flight (LF), Brownian motion (BM), and Random opposition-based learning (ROB) are all components of an improved version of the COA. Impressively, the suggested model correctly categorized 99.97% of the test data. The LFR-COA-DenseNet121-BC model outperformed other well-known models with a score of 99.97% accuracy, 99.96% sensitivity, and 99.9% specificity when compared to VGG16, VGG19, DenseNet201, InceptionV3, Xception, and MobileNet. The advantage of LFR-COA-DenseNet-BC was further shown by further comparison with COA-DenseNet121.

Qian et al. [30] introduced deep CNN based on the hybrid extreme learning machine (ELM) technique and improved the Chimp optimization algorithm (ChOA) for BC diagnosis. The success of the preprocessing stage is first evaluated using the Wiener and CALHE filters. Training on the CBIS-DDSM dataset followed after that using a modified pre-trained ZFNet. An ELM replaced the last few layers. The presentation included a technique for determining the optimal amount of structural layers to replace. ELM was eventually created to improve classification performance. The goal was achieved by combining four meta-heuristic optimization methods with an enhanced ChOA version.

Gutierrez et al. [31] discussed infrared imaging (IRI) Numerical Engine for BC detection. The method relies on Pennes's bioheat transport equations and employs a computational inverse heat transfer strategy. After following the institutional review board (IRB) policy and gaining informed permission, twenty-three patients with BC who have undergone biopsy will have their algorithms validated. Out of forty-four breasts, twenty-two were found to be cancer-free, according to the algorithm, and one lady had cancer in both breasts. The system also accurately identified the size and location of one tumour. The tumours are seen as metabolically active heat sources with high perfusion rates, which change the surface temperatures used in heat transfer models.

Huang et al. [32] deliberated the hybrid SqueezeNet and improved chef-based optimizer for BC diagnosis. A median filtering-based noise reduction technique is used first to eliminate the noise. In the next step, the Kapur approach is used to threshold the area of interest from the preprocessed pictures. Optimal feature extraction and selection are then devised to remove unnecessary features. An enhanced version of the Chef-Based Optimization (ICBO) algorithm provides the basis for its establishment. Finally, the diagnosis is completed by implementing a classification based on an ideal SqueezeNet model. Like the other classifiers, this one has been fine-tuned using the ICBO method. The method's efficacy is shown by simulations run on the MIAS database and contrasted with several state-of-the-art approaches.

The disadvantages highlighted for various DL methods applied to PET image BC, such as Xception-based DL and U-Net-based models, highlight the challenges in deploying these techniques in clinical settings. Issues like computational complexity, overfitting, and data quality and quantity sensitivity

indicate the need for robust optimization strategies, larger datasets, and efficient deployment protocols to ensure their practical utility in real-world healthcare scenarios. From the disadvantages mentioned earlier, such as susceptibility to overfitting, computational complexity, and sensitivity to data quality, it's evident that optimized DL is needed to mitigate these challenges and improve the practical applicability of DL models in healthcare, specifically for PET image BC analysis.

Optimization techniques can address these issues by fine-tuning model parameters, reducing overfitting through regularization methods, and optimizing computational efficiency for real-time deployment in clinical settings. Moreover, optimization enables the development of more interpretable models, enhances performance on limited datasets, and effectively ensures scalability to handle large volumes of heterogeneous data. Therefore, optimized DL plays a crucial role in overcoming the limitations associated with DL methods and maximizing their effectiveness in medical imaging applications like BC diagnosis using PET images.

3.Proposed methodology

This work introduces a novel approach called the DGWSMF for addressing the color digital images to identify impulsive noise reduction. It is designed to reduce noise while preserving image quality. The SAFCM clustering algorithm was employed to segment PET scan image datasets.

This technique leverages fuzzy logic and spatial information to accurately delineate affected regions within medical images, facilitating the analysis and diagnosis of medical conditions. Furthermore, to address the task of BC classification in PET images, an ODCSNN is proposed that combines the power of DL with SNNs, offering advantages in terms of computational efficiency and biological plausibility. Direct training of the network ensures end-to-end optimization for the BC classification task. To enhance the performance of ODCSNN, the ANFA for optimal selection of network weights effectively searches the weight space to find configurations that lead to higher classification accuracy. The architecture diagram of the proposed NeuroPET framework is presented in *Figure 1*.

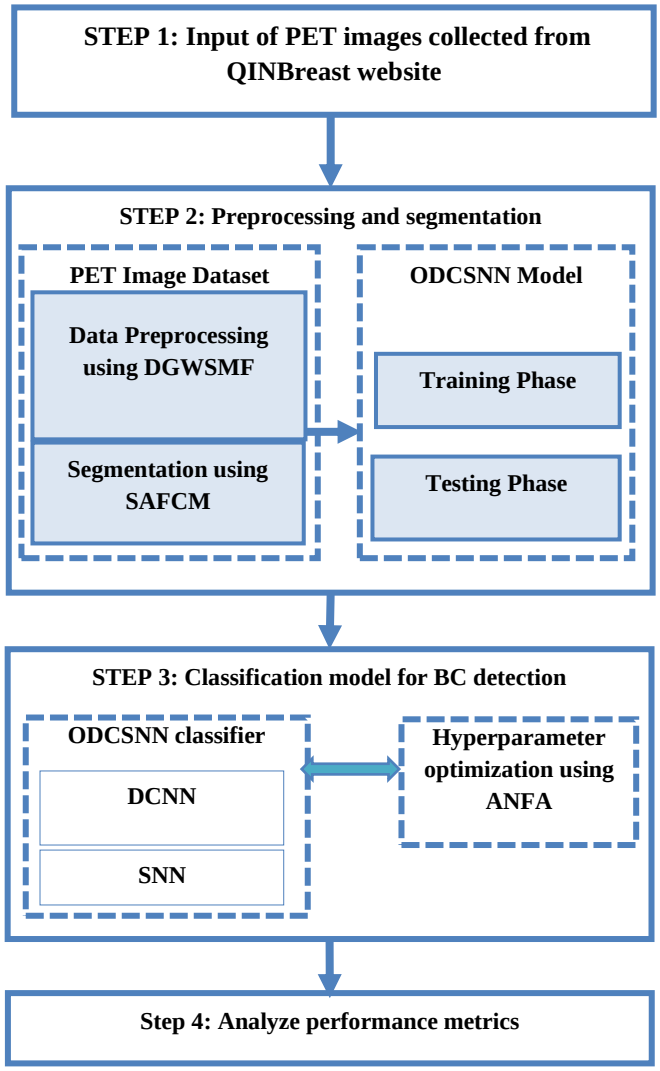

Figure 1 Architecture diagram of the proposed NeuroPET framework

3.1Dataset description

The quantitative imaging network (QIN)-breast dataset [33] was used for the experimentation. This dataset includes quantitative magnetic resonance (MR) images and longitudinal PET/CT scans that were mainly gathered to investigate therapy evaluation in BC in a pretreatment situation. Three crucial times were recorded: before the start of the treatment (t1), following the initial phase of medications (t2), and either the second round of treatment or the end of all therapies before operations (t3). A specially designed supporting device allowed patients to assume a prone position while acquiring PET/CT images to facilitate alignment with magnetic resonance imaging (MRI) data.

Distribution of benign and malignant cases: The dataset contains medical images (e.g., mammograms, MRI scans) of breast tissues from both benign (non-cancerous) and malignant (cancerous) cases. The distribution of benign and malignant cases may vary depending on the specific subset or version of the dataset. Generally, there tends to be a higher proportion of benign cases than malignant cases in medical imaging datasets due to the lower prevalence of BC.

Subject demographics: The dataset include information about the subjects' demographics, such as age, gender, ethnicity, and relevant medical history. Demographic information is essential for understanding how various factors may influence the detection and diagnosis of BC.

The dataset comprises 214 studies, encompassing 530 series and 100,835 images, with a collective image size of 11.286GB. It is publicly accessible through the Cancer Imaging Archive (TCIA) website. This dataset represents a significant asset for the medical imaging community, facilitating advancements in early treatment assessment methodologies and ultimately contributing to improved patient care and outcomes in BC management. By splitting the QIN-Breast dataset into training and testing subsets with an 80:20 ratio, researchers can effectively train and evaluate ML models while ensuring that they are trained on sufficient information and rigorously tested for their execution on hidden cases.

The dataset's properties are an essential factor impacting the efficiency of the NeuroPET system's algorithms. The DGWSMF, SAFCM, and ODCSNN algorithms learn more robust features and patterns from a large, diversified, high-quality dataset with precise labels. This enhances their performance in noise reduction, segmentation, and classification. Addressing issues like class imbalance and varying image resolutions improves the model's capacity to apply to clinical situations, making it more accurate and reliable in detecting BC.

3.2Image preprocessing using DGWSMF

The DGWSMF filter improves upon the switching median filter by incorporating adaptive weighting based on the local image characteristics. This adaptive weighting helps preserve edges and fine details while effectively reducing noise. The DGWSMF filter algorithm can be summarized as follows:

1. Set the size of a sliding window surrounding all the pixels in the image.
2. Calculate the median value of the intensities within the window.
3. Compute a weight for each pixel in the window based on its distance from the median value. Pixels closer to the median value are given higher weights.
4. Compute the weighted average of the window's pixel values to obtain the filtered value for the central pixel.
5. Repeat this process for each pixel in the image.

The enhanced adaptive weighted subspace method (EAWSM) filter introduces adaptive weights w_{ij} for each pixel in the window, which are calculated as follows in Equation 1:

$$w_{ij} = \frac{1}{1+\left(\frac{|Int_{ij}-MInt|}{Th\cdot\sigma}\right)^2} \quad (1)$$

Here, the intensity of the pixel at position (i,j) in the window can be represented as Int_{ij} is the intensity of the pixel at the position (i,j) in the window; $MInt$ is the median intensity value of the pixels, σ is the standard deviation of the pixel intensities in the window, Th is a user-defined parameter that controls the sensitivity of the weighting. Higher values of Th result in more aggressive weighting. The filtered value of the central pixel is then computed using the weighted average as per Equation 2:

$$\widehat{Int}_{ij} = \sum_{m,n} \frac{w_{m,n}\cdot Int_{mn}}{w_{m,n}} \quad (2)$$

Where the summation is performed over all pixels (m,n) in the window. By incorporating adaptive weights based on the local characteristics of the image, the EAWSM filter can effectively suppress noise while preserving edges and fine details, making it a valuable tool in image processing applications. Adjusting the parameter allows users to control the trade-off between noise reduction and edge preservation. Using radioactive tracers in PET scans results in significant background noise. The DCSNN uses state-of-the-art preprocessing methods such as anisotropic diffusion and Gaussian filtering to solve this. These approaches smooth the pictures by improving the input data quality while keeping essential features and edges. The model employs spike-timing-dependent plasticity (STDP) to mitigate noise, drawing on SNN's capabilities. STDP modifies synaptic weights according to spike timing to improve signal-to-noise ratio and noise filtering. This method shines when it comes to keeping essential

characteristics while reducing noise. The DCSNN's deep convolutional layers were trained to identify features in PET scan pictures. Convolutional filters look for patterns in metabolic activity to identify malignant cells. Gradually, the network captures high-level BC-related features via a sequence of pooling and convolutional layers.

3.3Segmentation using SAFCM clustering method

The SAFCM clustering algorithm is used for image segmentation, particularly in medical image analysis, such as PET scans. It is designed to partition an image into regions with similar characteristics, which is crucial in identifying affected regions in medical images. Here's an overview of how the SAFCM algorithm works:

Initialization: Choose the Number of clusters c and spatial neighbourhood matrix. Randomly initialize cluster centres.

Membership calculation: Calculate the membership degree of each pixel to each cluster. This is done using a fuzzy membership function, which determines the likelihood of a pixel belonging to each cluster. In SAFCM, this membership calculation is adapted to incorporate spatial information, meaning neighbouring pixels are likelier to belong to the same cluster. An image's key feature is the strong correlation between adjacent pixels. In simpler terms, there is a significant possibility that these adjacent pixels are part of a similar cluster because they have identical values. Although this spatial link is substantial for clustering, the typical FCM method fails to use it. To utilize the spatial data, a spatial function (SF) is expressed as in Equation 3,

$$SF_{ij} = \sum_{k \in sw} \mu_{ik} \times c, \quad (3)$$

Here, the number of cluster sizes can be symbolized as c, and the square window of $m \times n$ size centred on the x_j pixel in the spatial domain can be denoted as $sw(x_j)$. The probability of x_j joining ith cluster can be represented as SF_{ij}. The membership function indicates that.

Cluster center update: Update the cluster centers based on the membership values. This step adjusts the cluster centers better to represent the pixel intensities in their respective regions. When most of a pixel's neighborhood comprises members of similar clusters, the pixel's SF for that cluster is high. Membership function μ incorporates the SF in the following way as per Equation 4:

$$\mu'_{ij} = \frac{\mu_{ij}^{g} SF_{ij}^{h}}{\sum_{k=1}^{c} \mu_{kj}^{g} SF_{kj}^{h}} \quad (4)$$

Here, the parameters g and h regulate the significance; one function concerns the other. When a region is homogeneous, the SF only promotes the original membership, leading to an unchanging clustering outcome. However, this algorithm lessens the relative importance of a noisy cluster through the labels of its neighboring pixels for a noisy pixel. Consequently, rectifying false clouds or incorrectly identified pixels from noisy areas is simple.

Stopping Criterion: Check for convergence. This can be based on changes in cluster centers or membership values. If the algorithm has converged, exit; otherwise, return to step 2.

Output: After convergence, each pixel has a membership value for each cluster, indicating its likelihood of belonging to that cluster. These membership values can then segment the image into distinct regions, typically allocating each pixel to the cluster with the maximum membership value. Algorithm 1 shows the steps of SAFCM-based segmentation.

Algorithm 1: The algorithm steps of SAFCM-based segmentation

Input: PET scan image, Number of clusters (c), fuzziness parameter (m), stopping Criterion

Output: segmentation output of PET images

1. Initialize: Randomly initialize c and the spatial neighbourhood matrix
2. For iteration=1 to n, do
3. Calculate membership matrix μ:
4. For each pixel i:
5. for each cluster j:
6. Calculate the μ_{ij} using the spatial adaptation formula Equation 3
7. Update based on the distance between pixel i and cluster centre j
8. Normalize the membership values for each pixel using Equation 4
9. Update cluster centres:
10. For each cluster j:
11. Calculate the new cluster centre using the weighted average of pixel intensities
12. Update the cluster centre
13. Check for convergence:
14. Calculate the difference between old and new cluster centres
15. If the change in cluster centres is less than the stopping Criterion, the exit loop
16. End process

Display the segmented image based on the highest membership value for each pixel.

3.4Masses classification phase using ODCSNN

BC detection using an ODCSNN with direct training on PET images and subsequent weight optimization through the ANFA represents a cutting-edge medical imaging and artificial intelligence approach. PET images offer valuable insights into metabolic activity within breast tissue, which is crucial for identifying cancerous regions. Ultimately, the integration of ODCSNN with ANFA holds significant promise for advancing early detection and diagnosis of BC, offering clinicians a powerful tool to improve patient outcomes and treatment strategies. Algorithm 2 shows the steps of BC detection using the proposed ODCSNN. The ANFA algorithm aims to improve the network's performance by finding the best solution that optimizes model accuracy while minimizing classification error in the high-dimensional weight space. ANFA adjusts the learning rate dynamically during training. It decreases as convergence approaches to fine-tune weights and increases in the early stages to explore the weight space efficiently. The method modifies the momentum term based on gradient behaviour, increasing it when gradients are constant and decreasing it when they fluctuate.

Algorithm 2: The algorithm steps of BC detection using the proposed ODCSNN method

Input: PET image dataset with corresponding labels (0 for non-cancerous, 1 for cancerous)

Hyper Parameters: Number of layers (L), Number of neurons per layer (N), Number of training epochs (E), ANFA parameters

ODCSNN Training:

1. Initialize ODCSNN weights randomly.
2. Repeat for E epochs:
   a. For each PET image in the dataset:
      i. Feed the PET image into the ODCSNN.
      ii. Perform forward propagation through the network.
      iii. Compute the error among the network's output and the ground truth label.
      iv. Perform backward propagation (backpropagation) to update the network weights using gradient descent.
3. ODCSNN-trained weights are obtained after E epochs.

ANFA Weight Optimization:

1. Initialize a population of candidate weight configurations (nuts) randomly.
2. Repeat until convergence or maximum iterations are reached:
   a. Evaluate each nut's fitness by training ODCSNN with its weights and computing accuracy on a validation set.
   b. Select top-performing nuts based on fitness.
   c. Update the position of each nut based on ANFA rules:
      i. Move nuts towards better-performing regions.
      ii. Encourage exploration by introducing random perturbations.
   d. Repeat the process until convergence or maximum iterations are reached.

Output: Optimized weights for the ODCSNN obtained from ANFA.

DCSNN method: The proposed DCSNN structure, depicted in *Figure 2*, consists of a hierarchical arrangement of stacked convolutional (C) layers, a spatial-pooling (S) layer, a spiking neuron (SN) layer, and a fully connected (FC) layer. The C layers gradually extract characteristic information from complex input visual structures. First, low-level features like corners and edges are identified by the first C layer; later layers extract higher-level information from the activation maps of the previous layer. The training shared weight kernels via the offered unsupervised convolutional STDP learning technique facilitates hierarchical FE, with the learned data incorporated in the average spiking activity of the neurons producing the convolutional feature maps (FM).

Then, the S layer is used, which runs at a stride of two pixels at a time with a fixed 2×2 kernel. While maintaining local pixel correlations, the spatial-pooling technique reduces the (convolutional FM) CFM's dimensionality. Our method uses average pooling, with a threshold of 0.25 and each kernel weight set to 1. If any of the four input pixels spike during a kernel stride over a CFM, the matching neuron in the pooling FM produces an output spike. With little loss of spike data, this method efficiently decreases the CFM's dimensionality by a factor of two. Notably, the weight kernel used in the S process is still fixed and untrainable. By lowering the CFMs' dimensionality, S improves computation efficiency and grants network invariance to minor distortions and translations in the input data. The proposed DCSNN architecture described in the passage consists of several key components:

1. **Input layer:** The input layer receives the raw segmentation of input images, where each neuron in this layer typically represents a pixel or a group of pixels. Neurons represent individual pixels or regions of interest in the PET image. The input layer receives the PET image as a spatiotemporal signal, where the temporal dimension could represent different time frames of the scan.

2. **Convolutional layers (C)** extract distinctive features from the input image structures. The hierarchy of stacked C layers begins with low-level features, such as edges and corners in the first layer, and progresses to higher-level features in subsequent layers. The shared weight kernels are trained using an unsupervised convolutional STDP learning approach. The learned information is contained in the average spiking activity of the neurons within the CFMs.
3. Neurons represent individual pixels or regions of interest in the PET image. The spiking convolution operation involves convolving the input spikes with spiking filters to generate spiking FMs. The activation function used in SNs might involve spike generation once a specific threshold for the membrane potential is reached.

Spatial-pooling layer (S): A spatial-pooling layer follows the convolutional layers. The function of this layer is to reduce the convolutional FM dimension while maintaining the local correlation between the pixels. Average pooling with a fixed 2×2 kernel and a 2-pixel stride is used in this work. An output spike is produced if the four input pixels spike throughout a kernel stride across a CFM. This minimizes the loss of spike information while reducing the FM's dimensionality by a factor of two. S uses a fixed, non-trainable weight kernel. The advantages of S include:

- Increased computing effectiveness through CFM dimensional reduction.
- Making the network resistant to modest changes in the input structures' translations and distortions.

Spiking neuron layers: These layers consist of SNs, which model the behaviour of biological neurons. SNs accumulate input spikes over time and generate output spikes when a certain threshold is reached. The dynamics of SNs allow DCSNNs to process temporal information efficiently. The Leaky Integrate-and-Fire (LIF) neuron algorithm is a commonly used Spiking Neurons (SN) model. The following formulas can be used to characterize the LIF neuron's dynamics as per Equation 5:

Membrane Potential (V): $\tau_m \frac{dV}{dt} = -V(t) + R \cdot I(t)$ (5)

Here, the membrane resistance can be denoted as the input current to the neuron at time *t*, represented as $I(t)$, *and* V at time t, defined as $V(t)$. The membrane time constant can be represented as τ_m, which indicates the time it takes for the V to reach around 63.2% of its final value in response to a step input.

Spiking threshold (V_{th}): When it approaches the Vth, the neuron produces an output spike and resets the *V*.

Output spike: If $V(t) \geq V_{th}$, emit spike and reset $V(t)$ to a resting value

These equations govern the behaviour of individual neurons in an SNN. In a DCSNN, these SNs are arranged in layers and connected according to the network architecture, allowing for the processing of spatiotemporal data such as images or sequences.

Fully-connected (FC) layer: This layer typically follows the spatial pooling layer and performs classification or other relevant tasks based on the features extracted by the preceding layers. Finally, an FC (output) layer is incorporated with as many neurons as required for the specific identification task. After establishing complete interconnections with all the neurons that comprise the FMs in the previous S layer, each output neuron learns to infer input patterns by utilizing the high-level representations that have been recovered. A test pattern is categorized into the class indicated by the output neuron displaying the maximum spike count during the presentation interval. We apply competitive lateral inhibition among the output neurons throughout inference to improve the FC layer's recognition performance (*Figure 2*). All other output neurons' membrane potentials decrease with a constant inhibition factor when one of them fires. By reducing the spiking activity of neurons that recognize input patterns that share characteristics with the test patterns presented, these inhibitory connections enhance DCSNN's recognition abilities.

3.5ANFA-based hyperparameter tuning of DCSNN

Hyperparameter tuning is a crucial step in optimizing the performance of DCSNNs for tasks such as BC detection in PET images. ANFA is a metaheuristic algorithm inspired by the social behaviour of chipmunks, which can be applied to search for optimal hyperparameters efficiently. Using ANFA efficiently explores the hyperparameter space of a DCSNN and finds configurations that lead to improved performance in BC detection from PET images. This approach helps to automate the hyperparameter tuning process and can lead to more optimal network architectures and configurations.

Key hyperparameters tuned via ANFA include learning rate, number of layers, number of neurons per layer, kernel size, activation functions, and regularization parameters. A range of 0.001 to 0.0001 provided the optimal compromise between convergence speed and accuracy when the learning rate was changed from 0.0001 to 0.01. By experimenting with 64, 128, and 256 neurons per layer, this study found that 128 neurons per layer significantly improved accuracy without significantly raising computing costs. From 0.2 to 0.7, the DGWSMF weight was examined; 0.5 yielded promising results, while 0.7 increased the model's capacity to deal with noisy data and overall detection accuracy.

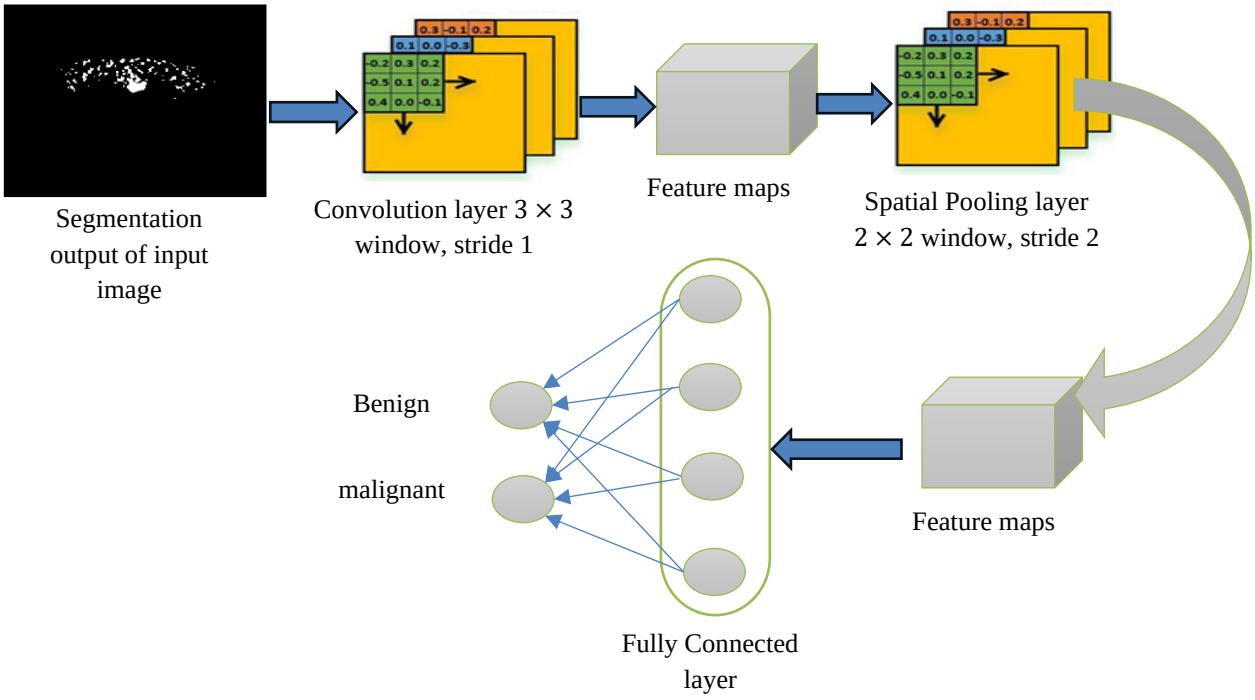

Figure 2 Architecture diagram of DCSNN

***The ANFA algorithm*:** This method imitates the soaring technique employed by southern flying chipmunks, an efficient means of travelling long distances for small mammals in forests of deciduous trees across Asia and Europe. Chipmunks travel across the forest for food during warm weather by flying from one tree to another. Acorn nuts are conveniently accessible to them for their everyday energy requirements. The best food source, hickory nuts, are then sought for and stored for the winter. In the winter, they get more complicated.

Initialize the algorithm parameters: Pop denotes the population size, the Number of decision variables can be symbolized as n, max denotes the maximum Number of iterations, the soaring constant SC and sf denotes the scaling factor, and the decision variables DV_{ub} and DV_{lb}, are the upper and lower bounds for these decision variables are the essential parameters of the ANFA. The ANFA method starts with these settings configured.

Initialize flying chipmunks' locations and their sorting: The search space randomly sets the positions of the flying chipmunks in the following Equation 6:

$$DV_{ij} = DV_{lb} + r_1(*) = (DV_{ub} - DV_{lb}), i, j = 1, 2, \dots, n \quad (6)$$

Here, the random Number in the interval [0, 1] with uniform distribution is denoted by $r_1()$. For hyperparameter tuning of a DCSNN for BC detection in PET images, the fitness function f could be defined based on the network's performance on a validation set using accuracy metrics. Subsequently, the position of the flying chipmunks' fitness value is used to sort the standard of food sources in an ascending sequence, as shown in Equation 7:

$$[sorted\_f, sorte\_index] = sort(f) \quad (7)$$

Three types of trees are characterized after the food supplies for all flying chipmunk positions are sorted: oak tree ot (food source: acorn nuts), hickory tree ht (food source: hickory nuts), and it represents the standard tree. The hickory nut tree DV_{ht} is considered the best food source (i.e., minimal f). The positions of the following three food sources are considered to be the oak nut trees (DV_{ot}), while the remaining trees are thought to be regular trees (DV_{nt}), as shown in Equations 8 to 10:

$$DV_{ht} = DV\big(sortex\_index(1)\big) \quad (8)$$

$$DV_{ot}(1:3) = DV\big(sortex\_index(2:4)\big) \quad (9)$$

$$DV_{nt}(1:NP-4) = DV\big(sortex\_index(5:NP)\big) \quad (10)$$

Predators impact flying chipmunks' natural behaviours when they find new areas, governed by hp the predator presence probability. Because of their wide dispersion and frequent separation from food sources, flying chipmunks are particularly vulnerable to attackers during their early seeking stage. The sites of flying chipmunks are near the food source; since they are still evolving, this is an ideal situation. In this instance, fewer predator risks are anticipated, and the flying chipmunk population's distribution region is getting smaller. Therefore, an adaptive hp that shifts as a function of the iteration number is selected as follows to improve the ANFA's exploitation capacity as per Equation 11:

$$hp = (\max hp - \min hp) \times \left(1 - \frac{it}{\max it}\right)^{10} + \min hp \quad (11)$$

The maximum and minimum hp can be denoted as $\max hp$ and $\min hp$ accordingly.

Create fresh destinations by soaring: Tree situations might occur following the active soaring procedure of flying chipmunks. Hickory nut trees are typically approached by flying chipmunks on acorn nut trees. The following can be utilized for generating the new positions as shown in Equation 12:

$$FS_{ot}^{new} = \begin{cases} DV_{ht}^{od} + sf * (sd)\big(DV_{ot}^{old} - DV_{ht}^{old}\big) * hp, & if\ r_1 \geq hp \\ random\ position, & otherwise \end{cases} \quad (12)$$

Here, the function on the interval [0, 1] can be symbolized as R, which yields a value from the uniform distribution. Soaring distance sd has been identified and ranges between 9 and 20 m in all cases. However, due to its magnitude, this value has the potential to significantly disrupt Equations 8–10, thereby compromising the algorithm's effectiveness. A scaling factor (SF) of 18 is selected for satisfactory algorithmic performance.

Check seasonal monitoring conditions: Seasonal fluctuations impact flying chipmunks' foraging behaviour. A seasonal monitoring criterion is added to avoid the algorithm being stuck in locally optimal solutions. First, at t, a seasonal constant (sc) and its minimum value are determined by Equations 13 and 14:

$$sc^t = \sqrt{\sum_{k=1}^{n}\big(DV_{ot,k}^t - DV_{nt,k}\big)^2}, \quad t = 1,2,3 \quad (13)$$

$$\min sc = \frac{10E-6}{365^{it/(\max it)/2.5}} \quad (14)$$

Subsequently, the condition of seasonal monitoring is assessed. If $sc^t < \min sc$, the winter ends, and flying chipmunks move their search space arbitrarily for food sources based on the DV provided in Equation 15.

$$DV_{nt}^{new} = DV_{lb} + \text{Levý (n)} \times (DV_{ub} - DV_{lb}) \quad (15)$$

Where most optimization algorithms can improve their capacity for global search by using the Levy distribution, an efficient mathematical mechanism [24] as per Equation 16:

$$\text{Levý}(x) = 0.01 \times \frac{r_2 \times \sigma}{|r_3|^{1/\beta}} \quad (16)$$

Here, the constant (ω = 1.5 in this work) can be denoted as ω, two functions that randomly select a value from the uniform distribution on the interval [0, 1] are represented as r_2 and r_3, and σ is computed as follows in Equation 17:

$$\sigma = \left(\frac{\Gamma(1+\omega) \times \sin\left(\frac{\pi\omega}{2}\right)}{\Gamma\left(\frac{(1+\omega)}{2}\right) \times \omega \times 2^{\left(\frac{(\omega-1)}{2}\right)}}\right)^{1/\beta} \quad (17)$$

Where $\Gamma(x) = (x-1)!$.

Stopping criterion: The method terminates if the maximum number of iterations is reached. Otherwise, the processes of generating new locations and evaluating the conditions of seasonal monitoring are carried out. Algorithm 3 provides the pseudocode of ANFA for hyperparameter tuning of DCSNN, while the flowchart is illustrated in *Figure 3*.

Algorithm 3: The pseudocode of ANFA for hyperparameter tuning of DCSNN

Input: parameters of ANFA and hyperparameters of DCSNN

Output: optimal hyperparameter value

Initialize the search space for hyperparameters and population of ANFA with random hyperparameter configurations within the search space
Repeat until convergence or maximum iterations are reached:
For each chipmunk:
Evaluate the fitness of the current hyperparameter configuration using the DCSNN
If the current fitness is better than the personal best fitness of the chipmunk:
Update the personal best position of the chipmunks to the current position
end if
end for
Determine the global best position among all chipmunks
for each chipmunk:
Update the velocity and position of the chipmunks based on their personal best and the global best positions
end for
Return the best hyperparameter configuration found during the search process.

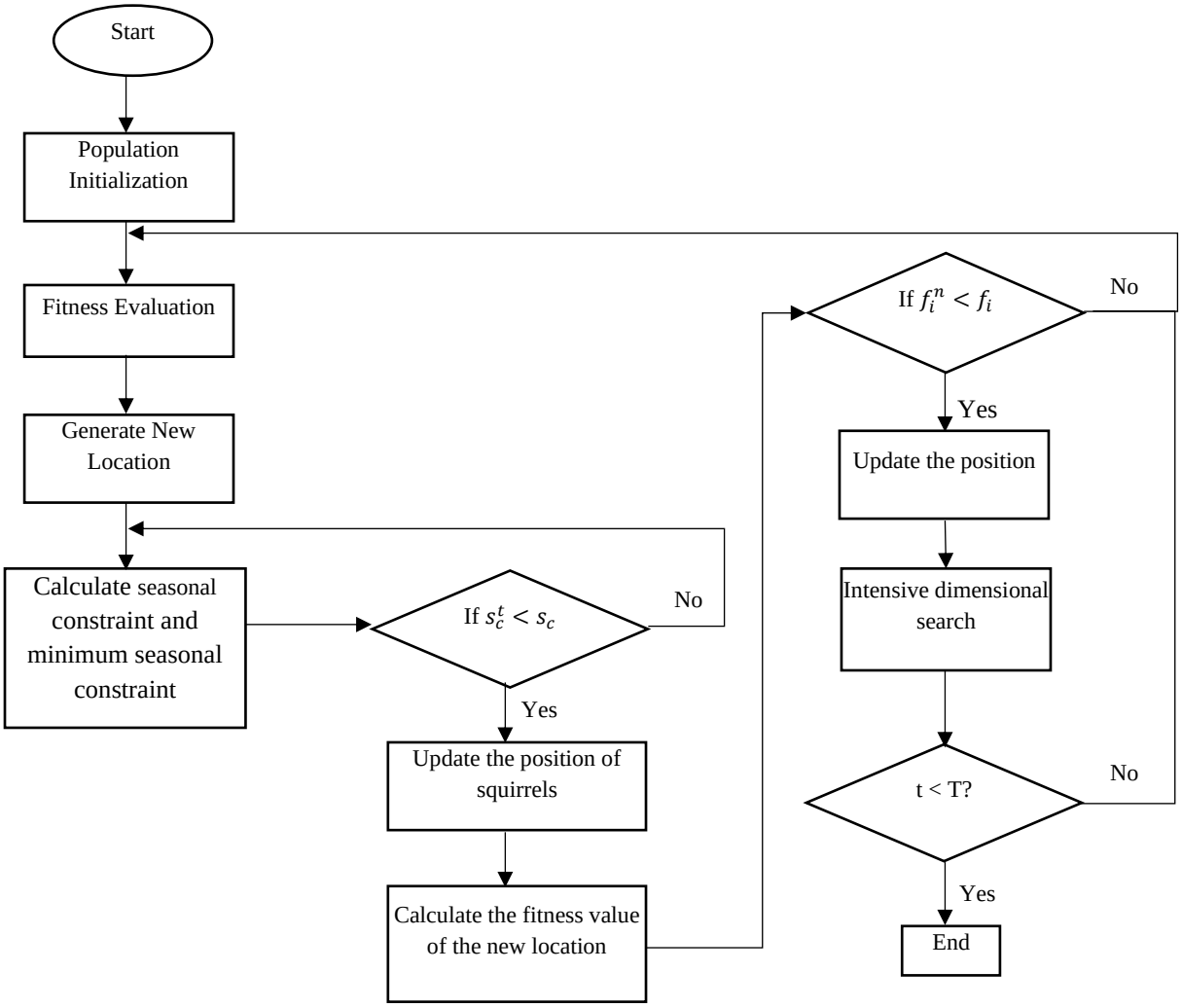

Figure 3 Flowchart of ANFA algorithm for optimizing the hyperparameters of the DCSNN model

Using robust statistical approaches, automated initial filtering procedures, or z-score analysis to identify and remove outlier values. This study collaborates with medical professionals to assess detected abnormalities and decide whether to keep them as unusual yet significant instances or send them out as errors. The quality of the image input into succeeding stages is improved by the DGWSMF, which intrinsically decreases noise and smoothes out minor irregularities. The filter changes between multiple

median filtering windows depending on the measured noise level to reduce noise while preserving high-frequency features (essential for spotting tumour edges). It uses intensity grading to give more weight to pixels in the filtering window that are less likely to constitute noise. The picture is now more transparent and of higher quality as a whole. This is where SAFCM comes in handy due to its capacity to deal with the fuzziness and ambiguity of medical pictures.

In contrast to more conventional clustering techniques, FCM indicates the extent to which each pixel is part of a cluster by assigning membership levels to them. From the PET scan pictures that have been segmented, the ODCSNN extracts high-level features using deep convolutional layers. These layers detect patterns linked to normal and cancerous tissues. Using the temporal dynamics of SNs, the characteristics that have been retrieved are transformed into spike trains, allowing for efficient processing. The network's capacity to identify small changes in metabolic activity that may indicate this spike-based representation enhances malignancy.

Several patterns and trends were discernible from the data examined to determine NeuroPET's efficacy in detecting BC. A notable pattern was the negative correlation between learning rate and model accuracy; specifically, accuracy decreased when learning rates were above 0.001, indicating that overshooting and less-than-ideal convergence resulted from higher rates. On the other hand, with lower learning rates (0.0001), convergence was more steady but slower; accuracy improved somewhat, but recall did not significantly increase. Increasing the filter weight (from 0.2 to 0.7) consistently increased accuracy and recall in the DGWSMF settings, another noteworthy trend. The results showed that the model could handle imaging data with more nuanced features and less noise after stronger filtering. The capacity of the model to detect intricate patterns in the data without substantial overfitting was also improved when the number of neurons per layer was raised, mainly when the number was raised from 64 to 128 neurons. Nevertheless, there is an ideal range for model complexity; increasing the number of neurons above 128 led to declining performance benefits.

4.Results and discussion

The QIN-breast dataset comprises 214 studies, encompassing 530 series and 100,835 images, with a collective image size of 11.286GB. It is publicly accessible through the TCIA website [33]. This dataset represents a significant asset for the medical imaging community, facilitating advancements in early treatment assessment methodologies and ultimately contributing to improved patient care and outcomes in BC management. To set up an experimental pipeline in MATLAB for training a DL model on the QIN-breast PET images dataset, an 80:20 split is employed for training and testing, respectively. Following data loading and preprocessing, which includes image resizing, normalization, and augmentation, the dataset is randomly divided into two subsets, ensuring a balanced distribution of cancerous and non-cancerous samples.

When it comes to detecting BC, the NeuroPET model may be severely affected by differences in imaging modalities and demographics. Several factors could influence the model's capacity to identify cancer, including the unique properties of various imaging modalities. Some imaging modalities, like mammograms, provide 2D pictures with a high resolution, while others, like MRI and PET scans, produce 3D images with different levels of sensitivity and contrast. The NeuroPET model may not work well with other modalities because of picture quality, noise, and texture variations. To illustrate, PET scans are very sensitive to metabolic activity, but their spatial resolution is often lower than MRI, which might result in less precise identification of tumour boundaries. Age, ethnicity, genetics, tumour features, and other patient population variables may also impact the model's accuracy. While mammography and ultrasound imaging of older people may reveal less thick tissue with more complicated tumour forms, younger women's denser breast tissue makes tumour detection more challenging. A further source of heterogeneity in the variables the model has to learn is the fact that tumour size, shape, and location might vary among different populations.

The NeuroPET framework is implemented, appropriately configuring training parameters such as learning rate and batch size. The model is then trained on the training subset, monitoring training progress using metrics like loss and accuracy. Subsequently, the trained model is evaluated on the testing subset to assess its performance metrics like accuracy, precision, and recall. Visualizations aid in interpreting the model's predictions and understanding its behaviour, facilitating insights for potential enhancements. As a result, the suggested framework primarily consists of two stages: the localization of masses and the classification of the

detected masses. *Figure 4* displays the input sample image along with the matching segmentation image. While some performance metrics are created to assess the efficacy of the mass classification, others are used to determine the accuracy of lesion detection. Here, the degree of accuracy of the algorithm in localizing cancers in breast mammograms was assessed using the intersection over union (IOU) measure in the following manner as per Equation 18:

$$IOU = \frac{AO}{AU} \quad (18)$$

As shown in Equation 18, AO is the overlap area, and AU is the union area. If the IOU is more significant than or equal to 0.5, the mass is considered accurately detected in this work; alternatively, the detection is disregarded. After a particular clssifier determines the tumour category of each localized mass, it is compared to the provided initial data to yield one of four possible outcomes. Initially, there is a benign mass that is labelled as malignant (false positive (FP)), followed by a benign mass identified as malignant true positive (TP), a malignant mass classed as benign FN, and finally, a benign mass classified as true unfavourable (TN). The confusion matrix, a fundamental metric for evaluating classification accuracy, primarily consists of four key components. The comparison methods include you only look once (YOLO)-V4 [21], DL-assisted efficient adaboost algorithm (DLA-EABA) [22], and oriented faster region-based convolutional neural network (OFRCNN) [23]. Likewise, TN, FN, FP, and TP were measured and used to compute the following metrics, as defined in Equations 19 to 22.

$$Precision = \frac{TP}{TP + FP} \quad (19)$$

$$Recall = \frac{TP}{TP + FN} \quad (20)$$

$$Overall\ accuracy = \frac{TP + TN}{TP + FN + TN + FP} \quad (21)$$

$$F1 - score = 2 * (Precision * Recall) / (Precision + Recall) \quad (22)$$

To examine the TP, TN, FP, and FN counts, this study constructed confusion matrices for the DGWSMF model across different thresholds. A significant trend highlighted by these matrices is a rise in FP and FN counts at extreme thresholds, which indicates difficulty balancing sensitivity and specificity. For example, when the threshold was lower, the model could detect most positive instances, resulting in high TP counts. However, this came at the expense of increasing FPs, which might have been avoided. At a higher threshold, on the other hand, TN counts decreased false alarms, but FN numbers increased, which might postpone the discovery of crucial BC. The model should be improved to increase diagnosis accuracy by addressing common misclassification patterns, such as the overlap of benign and malignant features. *Figure 4* shows the input image and the segmentation image of breast images. *Table 1* demonstrates that while each approach has its strengths, NeuroPET outperforms all others across key performance metrics, making it the most robust and reliable method based on these evaluation measures.

Table 1 The numerical outcome of suggested and current approaches depends on various performance metrics

Metrics	DLA-EABA	YOLO-V4	OFRCNN	NeuroPET
Accuracy (%)	80	91	92.60	95.02
Precision (%)	76.12	80	81.38	91.48
Recall (%)	82.12	83.40	93.62	95.06
F1-score (%)	78.10	81.66	87.07	93.24
Error (%)	20	9	7.3	4.9

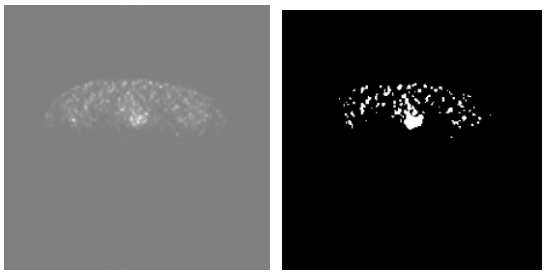

Figure 4 Input image and segmentation image

Figure 5, representing the objective space, typically illustrates the objective function plotted against the iterations. The optimal solution corresponds to the maximum point on this graph and thus solves the hyperparameter tuning of the proposed model. The parameter space graph in *Figure 5* illustrates how different combinations of parameters affect the algorithm's behavior and performance in finding optimal solutions. This graph might include axes representing various parameters (e.g., exploration

rate (x_1), exploitation rate (x_2), communication range (100)), and the contours or surfaces representing the algorithm's performance metrics (e.g., convergence speed, solution quality). The objective space graph shows the relationship between solutions and the objective function, while the parameter space graph depicts how different algorithm parameters influence the optimization process. Analyzing both graphs helps understand and fine-tune the ANFA for various optimization tasks.

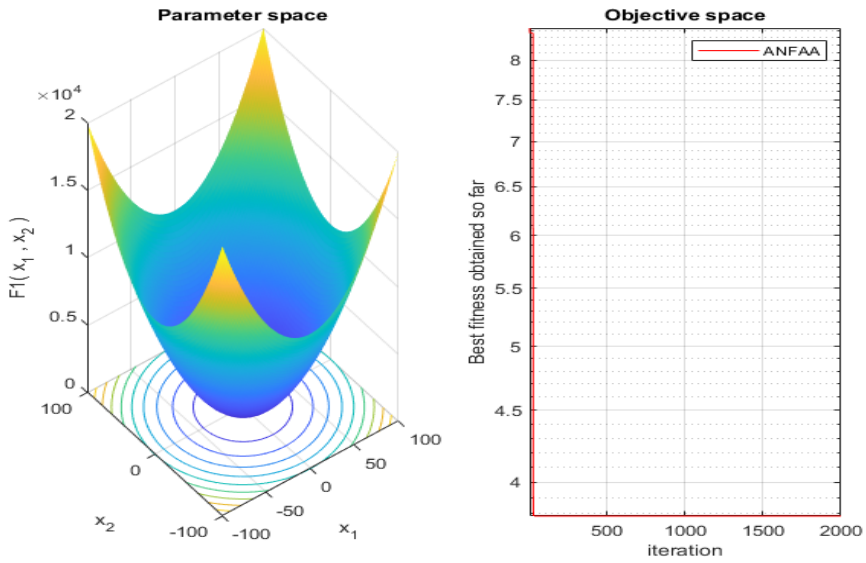

Figure 5 Parameter and objective space graph representation of ANFA

The comparative analysis in *Figure 6* illustrates the F1-score of suggested classifiers, including YOLO-V4, DLA-EABA, OFRCNN, and NeuroPET. The graph illustrates that the NeuroPET method achieves a significantly higher F1-score than the other methods, reaching 93.24%, demonstrating its exceptional accuracy in detecting BC. In contrast, the F1-scores of YOLO-V4, DLA-EABA, and OFRCNN are 81.66%, 78.10%, and 87.07%, respectively.

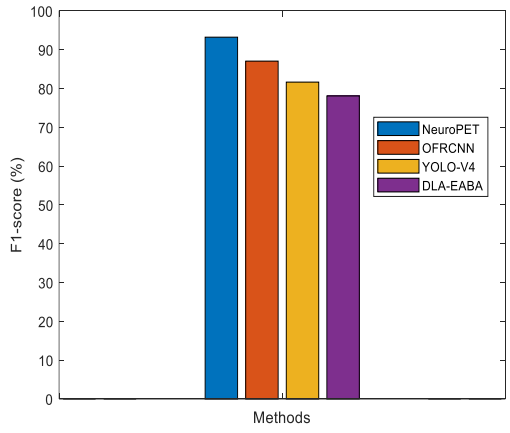

Figure 6 Scalability evaluation of the proposed model and benchmark models based on F1-score

The precision comparison results among the YOLO-V4, DLA-EABA, OFRCNN, and NeuroPET classifiers are presented in *Figure 7*. The proposed NeuroPET method demonstrates a notably higher precision rate than the existing methods, achieving 91.48%.

In contrast, the precision rates of the existing approaches are 80% for YOLO-V4, 76.12% for DLA-EABA, and 81.38% for OFRCNN. The ODCSNN architecture is specifically designed to effectively capture and represent complex features in PET images for BC classification. By leveraging deep convolutional layers, the network learns hierarchical representations that enable it to accurately distinguish between cancerous and non-cancerous regions with high precision.

This study utilized the precision-recall (PR) curve and the receiver operating characteristic (ROC) curve to evaluate the performance of the DGWSMF model, addressing potential dataset imbalance concerns.The PR curve further explores the model's sensitivity to positive instances by focusing on the balance between recall and accuracy. In contrast, the ROC curve emphasizes the trade-off between accurate positive and false favorable rates across thresholds.

Although accuracy decreased due to increased FP, the model showed better recall at lower thresholds, suggesting it successfully caught the majority of positive instances. The model's selectivity led to a considerable improvement in accuracy at higher thresholds at the expense of recall. Excellent performance was achieved even with an unbalanced dataset by analyzing the PR curve and identifying the threshold that provided the ideal balance for the target application.

The recall comparison results for the YOLO-V4, DLA-EABA, OFRCNN, and NeuroPET classifiers demonstrate that the proposed NeuroPET model achieves the highest recall rate of 95.06%, highlighting its superior capability in accurate detection and recognition.

Among the existing approaches, YOLO-V4, DLA-EABA, and OFRCNN achieve recall rates of 83.4%, 82.12%, and 93.62%, respectively. These results indicate that the proposed NeuroPET model outperforms previous techniques in disease recognition accuracy.

The high recall achieved by NeuroPET can be attributed to its comprehensive feature learning capabilities, direct training for BC classification, optimal weight selection using ANFA, and robust segmentation provided by SAFCM. Additionally, the integration of SNN dynamics enables the model to capture temporal dependencies in input data, further enhancing its performance (*Figure 8*).

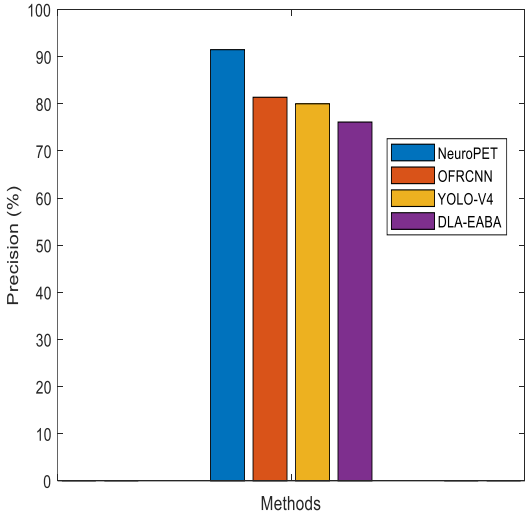

Figure 7 Scalability evaluation of the proposed model and benchmark models based on precision

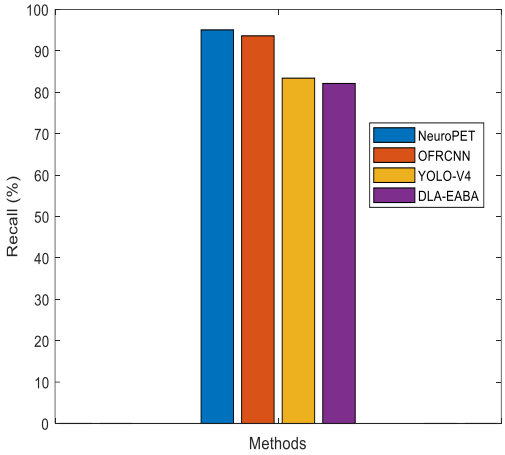

Figure 8 Scalability evaluation of the proposed model and benchmark models in terms of recall

Figure 9 presents an accuracy comparison for BC detection using YOLO-V4, DLA-EABA, OFRCNN, and NeuroPET classifiers. NeuroPET achieves the highest accuracy at 95.02%, surpassing YOLO-V4 (91%), DLA-EABA (80%), and OFRCNN (92.60%). Its superior performance is attributed to ODCSNN for BC classification, ANFA-based optimal weight selection, and DGWSMF preprocessing, which enhances data quality by removing noise. Additionally, SAFCM clustering improves segmentation accuracy. This holistic integration enables NeuroPET to deliver robust and precise BC detection in PET images, demonstrating its effectiveness over existing methods.

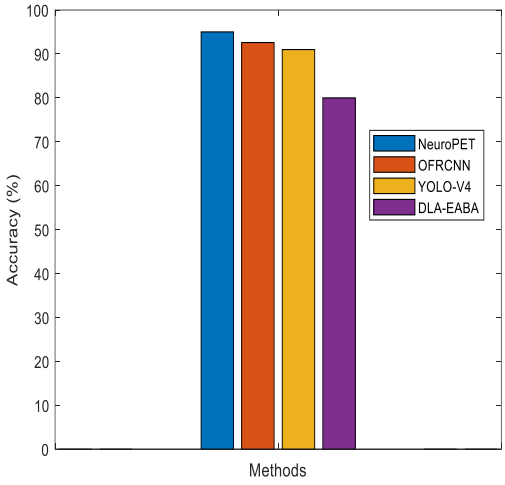

Figure 9 Scalability evaluation of the proposed model and benchmark models in terms of accuracy

Figure 10 presents a comparison of error rates for BC detection using YOLO-V4, DLA-EABA, OFRCNN, and NeuroPET classifiers. Among these, NeuroPET achieves the lowest error rate of 4.97, demonstrating its superior efficiency in accurate detection. In contrast, the error rates for YOLO-V4, DLA-EABA, and OFRCNN are 9, 20, and 7.3960, respectively. The low error rate of NeuroPET is attributed to its integration of ODCSNN, which enhances PET image analysis by extracting relevant features while reducing computational complexity, leading to more precise BC detection.

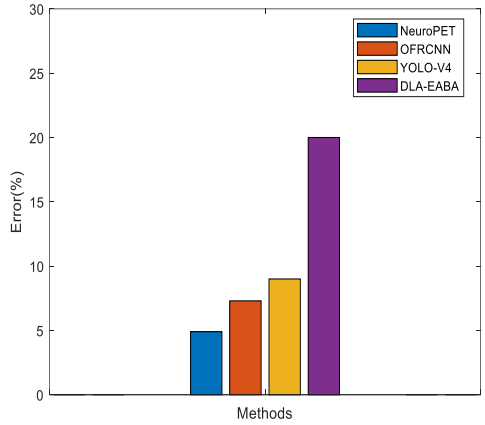

Figure 10 Scalability evaluation of the proposed model and benchmark models based on error rate

Figure 11 presents a comparative analysis of the ROC curves for NeuroPET, YOLO-V4, DLA-EABA, and OFRCNN, evaluating their performance in BC detection. The ROC curve plots the True Positive Rate (TPR or Sensitivity) against the False Positive Rate (FPR = 1 - Specificity) across varying decision thresholds, illustrating each model's ability to differentiate between cancerous and non-cancerous cases. The AUC quantifies the overall discriminative power, where a higher AUC signifies superior classification performance. According to the figure, NeuroPET exhibits the highest AUC, outperforming YOLO-V4, DLA-EABA, and OFRCNN. This indicates that NeuroPET achieves a more optimal trade-off between sensitivity (detecting cancer cases accurately) and specificity (correctly rejecting non-cancer cases) across all threshold settings. The steeper curve of NeuroPET further highlights its ability to maintain high TPR while minimizing FPR, reinforcing its robustness in BC classification. Additionally, the comparative ROC trends suggest that OFRCNN, YOLO-V4, and DLA-EABA demonstrate relatively lower classification efficacy, making NeuroPET the most reliable model for accurate and efficient BC detection.

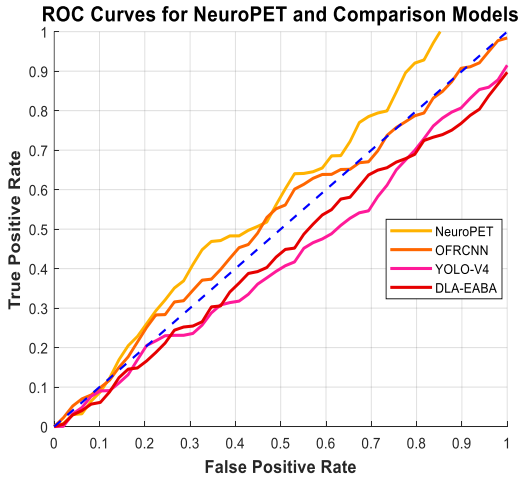

Figure 11 Comparison of ROC curves for BC detection using NeuroPET, YOLO-V4, DLA-EABA, and OFRCNN

Figure 12 provides a visual representation of classification outcomes, displaying counts of True Positives (TP = 3,690), False Positives (FP = 193), True Negatives (TN = 44,271), and False Negatives (FN = 2,022). The model demonstrates high specificity with a large TN count, effectively identifying non-cancer cases. While the low FP count minimizes unnecessary concerns, the high FN count (2,022) remains a critical issue, as missed cancer diagnoses can have severe consequences. This highlights the need for further model optimization to reduce FNs and improve detection sensitivity in medical diagnosis.

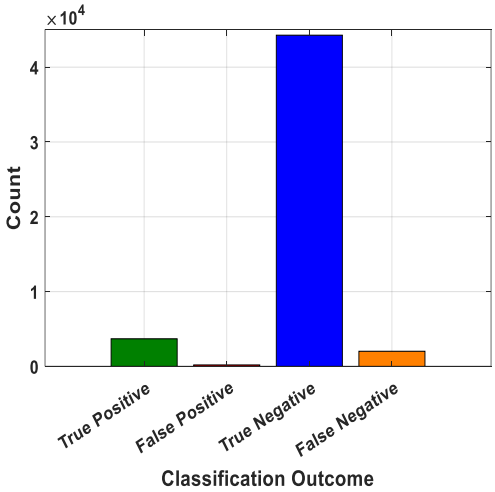

Figure 12 Graph for TPs, FPs, TNs, and FNs of cancer classification

This work presented a comprehensive framework, NeuroPET, for accurate classification of BC in PET images, addressing various preprocessing, segmentation, and classification challenges. The performance of NeuroPET, notably achieving a remarkable accuracy of 95.02% using the gradient surrogate method, highlights its potential as a state-of-the-art solution for BC detection. YOLO-V4, DLA-EABA and OFRCNN are the comparison methods. However, potentially limiting the model's value across multiple clinical situations is the risk of overfitting specific datasets and poor generalizability to new, unknown data from other populations or imaging technologies. Exploring novel neural network structures or incorporating attention mechanisms may enhance the model's capture of subtle features relevant to BC detection. Additionally, fine-tuning parameters and researching alternative methodologies may improve performance in the preprocessing and segmentation stages.

DGWSMF differs from conventional median filters by adjusting to the image's local intensity gradients, allowing for more accurate noise reduction while protecting important features and edges. Assigning membership levels to pixels allows SAFCM's fuzzy clustering technique to provide more detailed segmentation, successfully handling the inherent ambiguity in medical images. Processing that is both efficient and inspired by nature is made possible by transforming features into spike trains, which use the temporal dynamics of SNs.

Selecting the optimal hyperparameters, including the learning rate, number of neurons per layer, and DGWSMF settings, plays a crucial role in enhancing the prediction accuracy of the NeuroPET model. For instance, changing the learning rate from 0.0001 to 0.01 affected the model's performance. A lower learning rate (0.0001) resulted in slower convergence but somewhat better precision, while a higher learning rate (0.01) led to a drop in accuracy due to overshooting.

Additionally, increasing the number of neurons per layer improved the model's accuracy by enabling it to capture more complex information. However, the performance improvements diminished beyond a certain point. Higher DGWSMF filter weights (e.g., 0.7) achieved the best performance by effectively reducing input data noise enhancing accuracy, precision, and recall. Conversely, smaller filter weights (e.g., 0.2) resulted in poorer performance, as insufficient filtering hindered the model's ability to detect subtle cancer traits.

Limitations

Some of the study limitations are as under:

- Fine-tuning hyperparameters is essential for achieving optimal BC diagnosis, with particular emphasis on the DGWSMF filter, which plays a crucial role in enhancing model performance. However, the generalization of the model may be limited due to dataset constraints, necessitating validation on larger, multi-center datasets.
- While the DGWSMF is designed to reduce impulsive noise, real-world PET images may contain diverse noise types and artifacts. Therefore, NeuroPET's robustness under varying noise conditions, imaging artifacts, or scanner performance fluctuations requires further assessment.
- Another limitation is that NeuroPET has primarily been validated on specific datasets, potentially limiting its generalizability to real-world clinical settings.
- Although a high AUC confirms that NeuroPET effectively distinguishes between cancerous and non-cancerous cases, relying solely on a single performance metric is insufficient. A detailed error analysis highlights the need to further minimize false negatives, ensuring comprehensive cancer detection. Even with high precision and overall accuracy, prioritizing sensitivity improvements is essential to maximize early cancer diagnosis and reduce the risk of missed cases.

A complete list of abbreviations is listed in *Appendix I.*

5.Conclusion

This work introduces NeuroPET, a comprehensive framework for accurate BC classification in PET images, effectively addressing challenges in preprocessing, segmentation, and classification. The proposed DGWSMF efficiently removes impulsive noise from color digital images, while the SAFCM clustering algorithm ensures precise segmentation of affected regions. Additionally, ODCSNN provides a robust architecture for direct BC classification, with ANFA optimizing network weights to enhance accuracy. NeuroPET's high accuracy (95.02%) using the gradient surrogate method demonstrates its potential as a state-of-the-art BC detection solution. Future research could focus on expanding its applicability, real-time optimization, and integration of advanced techniques for enhanced performance.

Acknowledgment
None.

Conflicts of interest
The authors have no conflicts of interest to declare.

Data availability
The QIN-BREAST dataset utilized in this study is publicly accessible and can be found at https://www.cancerimagingarchive.net/collection/qin-breast/

Author's contribution statement
Conceptualization, methodology, data collection and analysis, resources, writing-original draft preparation, writing-review, and editing – **S. Tharani;** Supervision- **R. Khanchana.**

References
[1] Rai R, Tripathi V. An overview of breast cancer epidemiology, risk factors, classification, genetics, diagnosis and treatment. Vantage Journal of Thematic Analysis. 2023; 4:45-67.
[2] Wilkinson L, Gathani T. Understanding breast cancer as a global health concern. The British Journal of Radiology. 2022; 95(1130):1-3.
[3] Chamberlin MD. Global oncology: disparities, outcomes and innovations around the globe. An Issue of Hematology/Oncology Clinics of North America, E-Book. Elsevier Health Sciences; 2023.
[4] Nayyar S, Chakole S, Taksande AB, Prasad R, Munjewar PK, Wanjari MB, et al. From awareness to action: a review of efforts to reduce disparities in breast cancer screening. Cureus. 2023; 15(6):1-11.
[5] Sangwan RK, Huda RK, Panigrahi A, Toteja GS, Sharma AK, Thakor M, et al. Strengthening breast cancer screening program through health education of women and capacity building of primary healthcare providers. Frontiers in Public Health. 2023; 11:1-10.
[6] Castorina L, Comis AD, Prestifilippo A, Quartuccio N, Panareo S, Filippi L, et al. Innovations in positron emission tomography and state of the art in the evaluation of breast cancer treatment response. Journal of Clinical Medicine. 2023; 13(1):1-20.
[7] Cecil K, Huppert L, Mukhtar R, Dibble EH, O'brien SR, Ulaner GA, et al. Metabolic positron emission tomography in breast cancer. PET Clinics. 2023; 18(4):473-85.
[8] Fowler AM, Miyake KK, Nakamoto Y. Clinical applications of dedicated breast positron emission tomography. PET Clinics. 2024; 19(1):105-17.
[9] Xu K, Kang H. A review of machine learning approaches for brain positron emission tomography data analysis. Nuclear Medicine and Molecular Imaging. 2024; 58(4):203-12.
[10] Satoh Y, Imokawa T, Fujioka T, Mori M, Yamaga E, Takahashi K, et al. Deep learning for image classification in dedicated breast positron emission tomography (dbPET). Annals of Nuclear Medicine. 2022; 36(4):401-10.
[11] Perron J, Ko JH. Review of quantitative methods for the detection of Alzheimer's disease with positron emission tomography. Applied Sciences. 2022; 12(22):1-32.
[12] Balkenende L, Teuwen J, Mann RM. Application of deep learning in breast cancer imaging. In seminars in nuclear medicine 2022 (pp. 584-96). WB Saunders.
[13] Gu B, Yang Z, Du X, Xu X, Ou X, Xia Z, et al. Imaging of tumor stroma using 68Ga-FAPI PET/CT to improve diagnostic accuracy of primary tumors in head and neck cancer of unknown primary: a comparative imaging trial. Journal of Nuclear Medicine. 2024; 65(3):365-71.
[14] Sherman ME, Vierkant RA, Winham SJ, Vachon CM, Carter JM, Pacheco-spann L, et al. Benign breast disease and breast cancer risk in the percutaneous biopsy era. JAMA surgery. 2024; 159(2):193-201.
[15] Inglese M, Ferrante M, Duggento A, Boccato T, Toschi N. Spatiotemporal learning of dynamic positron emission tomography data improves diagnostic accuracy in breast cancer. IEEE Transactions on Radiation and Plasma Medical Sciences. 2023; 7(6):630-7.
[16] Khodabakhshi Z, Amini M, Hajianfar G, Oveisi M, Shiri I, Zaidi H. Dual-centre harmonised multimodal positron emission tomography/computed tomography image radiomic features and machine learning algorithms for non-small cell lung cancer histopathological subtype phenotype decoding. Clinical oncology. 2023; 35(11):713-25.
[17] Qiao X, Jiang C, Li P, Yuan Y, Zeng Q, Bi L, et al. Improving breast tumor segmentation in PET via attentive transformation based normalization. IEEE Journal of Biomedical and Health Informatics. 2022; 26(7):3261-71.
[18] Imokawa T, Satoh Y, Fujioka T, Takahashi K, Mori M, Kubota K, et al. Deep learning model with collage images for the segmentation of dedicated breast positron emission tomography images. Breast Cancer. 2023:1-8.
[19] Tsukijima M, Teramoto A, Kojima A, Yamamuro O, Tamaki T, Fujita H. A position-adaptive noise-reduction method using a deep denoising filter bank for dedicated breast positron emission tomography images. Physical and Engineering Sciences in Medicine. 2024; 47(1):73-85.
[20] Sueoka S, Sasada S, Masumoto N, Emi A, Kadoya T, Okada M. Performance of dedicated breast positron emission tomography in the detection of small and low-grade breast cancer. Breast Cancer Research and Treatment. 2021; 187:125-33.
[21] Yurdusev AA, Adem K, Hekim M. Detection and classification of microcalcifications in mammograms images using difference filter and Yolov4 deep learning model. Biomedical Signal Processing and Control. 2023; 80(2):104360.
[22] Nogales A, Perez-lara F, García-tejedor ÁJ. Enhancing breast cancer diagnosis with deep learning and evolutionary algorithms: a comparison of approaches using different thermographic imaging

treatments. Multimedia Tools and Applications. 2024; 83(14):42955-71.
[23] Singh L, Alam A. An efficient hybrid methodology for an early detection of breast cancer in digital mammograms. Journal of Ambient Intelligence and Humanized Computing. 2024; 15(1):337-60.
[24] Thakur A, Gupta M, Sinha DK, Mishra KK, Venkatesan VK, Guluwadi S. Transformative breast cancer diagnosis using CNNs with optimized reduceLROnplateau and early stopping enhancements. International Journal of Computational Intelligence Systems. 2024; 17(1):1-18.
[25] Munshi RM, Cascone L, Alturki N, Saidani O, Alshardan A, Umer M. A novel approach for breast cancer detection using optimized ensemble learning framework and XAI. Image and Vision Computing. 2024; 142:104910.
[26] Chugh G, Kumar S, Singh N. TransNet: a comparative study on breast carcinoma diagnosis with classical machine learning and transfer learning paradigm. Multimedia Tools and Applications. 2024; 83(11):33855-77.
[27] Raza A, Ullah N, Khan JA, Assam M, Guzzo A, Aljuaid H. DeepBreastCancerNet: a novel deep learning model for breast cancer detection using ultrasound images. Applied Sciences. 2023; 13(4):1-19.
[28] Sahu A, Das PK, Meher S. High accuracy hybrid CNN classifiers for breast cancer detection using mammogram and ultrasound datasets. Biomedical Signal Processing and Control. 2023; 80(1):104292.
[29] Emam MM, Houssein EH, Samee NA, Alohali MA, Hosney ME. Breast cancer diagnosis using optimized deep convolutional neural network based on transfer learning technique and improved coati optimization algorithm. Expert Systems with Applications. 2024; 255:124581.
[30] Qian L, Bai J, Huang Y, Zeebaree DQ, Saffari A, Zebari DA. Breast cancer diagnosis using evolving deep convolutional neural network based on hybrid extreme learning machine technique and improved chimp optimization algorithm. Biomedical Signal Processing and Control. 2024; 87:105492.
[31] Gutierrez C, Owens A, Medeiros L, Dabydeen D, Sritharan N, Phatak P, et al. Breast cancer detection using enhanced IRI-numerical engine and inverse heat transfer modeling: model description and clinical validation. Scientific Reports. 2024; 14(1):1-17.
[32] Huang Q, Ding H, Effatparvar M. Breast cancer diagnosis based on hybrid SqueezeNet and improved chef-based optimizer. Expert Systems with Applications. 2024; 237:121470.
[33] https://www.cancerimagingarchive.net/collection/qin-breast/. Accessed 25 January 2025.

S. Tharani earned her BCA, M.Sc. in Computer Science, and M.Phil from Sri Ramakrishna College of Arts and Science for Women. She is currently pursuing a Ph.D. in Data Mining. She was awarded a gold medal for securing the highest university ranking in Computer Science and also received the Bharathiar University Zindal Silver Jubilee Award. She has authored several books and is a lifetime member of multiple professional organizations.
Email: Vtharani1811@gmail.com

Dr. R. Khanchana is an Associate Professor in the Department of Computer Science at Sri Ramakrishna College of Arts & Science for Women. She has been associated with the institution for the past 15 years. She earned her Ph.D. in Computer Science from Karpagam University in 2014. Her research interests include Data Mining, Networking, the Internet of Things (IoT), and Big Data. Dr. Khanchana has published books on Amazon, with her most recent publication focusing on Data Mining. In 2017, she received funding assistance for a sponsored Research and Development project from the University Grants Commission (UGC). She has been actively involved in research supervision since 2010 and has guided Ph.D. scholars in their research.
Email: khanchanacs@srcw.ac.in

Appendix I

S. No.	Abbreviation	Description
1	ANFA	Adaptive Nut-Finding Algorithm
2	AT	Attentive Transformation
3	AUC	Area Under the Curve
4	BC	Breast Cancer
5	BM	Brownian Motion
6	CFM	Convolutional Feature Map
7	ChOA	Chimp Optimization Algorithm
8	CNN	Convolutional Neural Networks
9	COA	Coati Optimization Algorithm
10	dbPET	Dedicated Breast Positron Emission Tomography
11	DCNN	Deep Convolutional Neural Networks
12	DFE	Deep Feature Extraction
13	DGWSMF	Dynamic Grade Weighted Switching Median Filter
14	DL	Deep Learning
15	EAWSM	Enhanced Adaptive Weighted Subspace Method
16	ELM	Extreme Learning Machine
17	Faster R-CNN	Faster Region-Based Convolution Neural Network
18	FE	Feature Extraction
19	FM	Feature Maps
20	FN	False Negative
21	FP	False Positives
22	ICBO-Chef	Based Optimization
23	IOU	Intersection Over Union
24	IRB	Institutional Review Board

25	IRI	Infrared Imaging
26	LF	Lévy Flight
27	LR	Logistic Regression
28	MI	Molecular Imaging
29	MIP	Maximum Intensity Projection
30	ML	Machine Learning
31	MRI	Magnetic Resonance Imaging
32	NSCLC	Non-Small Cell Lung Cancer
33	ODCSNN	Optimal Deep Convolutional Spiking Neural Network
34	PET	Positron Emission Tomography
35	QIN	Quantitative Imaging Network
36	ReLu	Rectifier Linear Unit
37	RF	Random Forest
38	R-FCN	Region-Based Fully Convolutional Network
39	ROB	Random Opposition-Based Learning
40	ROC	Receiver Operating Characteristic
41	SAFCM	Spatial Adaptive Fuzzy C-Means
42	SF	Spatial Function
43	SN	Spiking Neurons
44	SNN	Spiking Neural Networks
45	SSD	Single Shot Detector
46	STDP	Spike-Timing-Dependent Plasticity
47	SVM	Support Vector Machines
48	TCIA	The Cancer Imaging Archive
49	TN	True Negative
50	TP	True Positive
51	VGG	Visual Geometry Group
52	WBPET	Whole-Body Positron Emission Tomography
53	XAI	Explainable Artificial Intelligence
54	XGB	eXtreme Gradient Boost
55	YOLO	You Only Look Once